PHOTONICS Research

# Spectrally multiplexed indistinguishable single-photon generation at telecom-band

Hao Yu,[1,2,†] Chenzhi Yuan,[1,†] Ruiming Zhang,[1] Zichang Zhang,[1] Hao Li,[3] You Wang,[1,4] Guangwei Deng,[1] Lixing You,[3] Haizhi Song,[1,4,8] Zhiming Wang,[1,5,9] Guang-Can Guo,[1,6] and Qiang Zhou[1,6,7,*]

[1]Institute of Fundamental and Frontier Sciences, University of Electronic Science and Technology of China, Chengdu 610054, China
[2]Institut national de la recherche scientifique-Centre Énergie, Matériaux et Télécommunications (INRS-EMT), Varennes, Quebec J3X 1S2, Canada
[3]Shanghai Institute of Microsystem and Information Technology, Chinese Academy of Sciences, Shanghai 200050, China
[4]Southwest Institute of Technical Physics, Chengdu 610041, China
[5]Shenzhen Institute for Quantum Science and Engineering, Southern University of Science and Technology, Shenzhen 518055, China
[6]CAS Key Laboratory of Quantum Information, University of Science and Technology of China, Hefei 230026, China
[7]School of Optoelectronic Science and Engineering, University of Electronic Science and Technology of China, Chengdu 610054, China
[8]e-mail: hzsong1296@163.com
[9]e-mail: zhmwang@gmail.com
*Corresponding author: zhouqiang@uestc.edu.cn

Received 15 December 2021; revised 31 March 2022; accepted 2 April 2022; posted 4 April 2022 (Doc. ID 450731); published 20 May 2022

**Heralded single-photon source (HSPS) intrinsically suffers from the trade-off between the heralded single-photon rate and the single-photon purity. To break through this trade-off, one can apply multiplexing technology in different degrees of freedom that significantly improves the performance of the HSPS. Here, we propose a 1.5 μm chip-scale HSPS on lithium niobate on insulator by employing spectral multiplexing and active feed-forward spectral manipulating, and we demonstrate a proof-of-principle experiment with discrete fiber-based components. With continuous-wave laser pumping and three spectral modes multiplexed, our experimental results show that the spectral multiplexing improves the heralded single-photon rate by near threefold while keeping the $g^{(2)}(0)$ as low as $0.0006 \pm 0.0001$ at a measured single-photon rate of 3.1 kHz. By measuring the joint spectral intensity, we show that the spectral multiplexing and feed-forward control effectively erase the frequency correlation of photon pairs. Moreover, we implement the Hong–Ou–Mandel interference between the spectrally multiplexed single photons and photons from an independent weak coherence source, which indicates that the multiplexed single photons are highly indistinguishable after the spectral manipulation. Our results pave a way for on-chip scalable and high-performance HSPS with spectral multiplexing toward deterministic single-photon emission.** 

https://doi.org/10.1364/PRJ.450731

## 1. INTRODUCTION

Single-photon source is an essential element in photonic implementations of quantum technologies, which ideally emits single photons in a pure, deterministic, and indistinguishable manner that can ensure several potential applications such as fundamental investigations of the quantum nature of light [1,2], security communication [3,4], exponentially enhanced calculation [5], and high accuracy measurement [6]. To make single-photon emission more applicable for wide-spread deployment in quantum techniques, two different avenues have been paved, which are based on single emitters [7] and spontaneous non-linear parametric processes, respectively. The first one is capable of emitting single photons deterministically, but it needs complex fabrication processes and is difficult to operate at room temperature. The second pathway is the heralded single-photon source (HSPS) [8], which is based on correlated photon pairs generated from spontaneous parametric down-conversion (SPDC) or spontaneous four-wave mixing. The detection of one of the photons in the photon pair, the heralding photon, indicates the existence of its twin photon, the heralded photon. Such HSPSs are experimentally convenient, emission wavelength flexible, and most importantly, highly indistinguishable. However, the spontaneous non-linear parametric processes bring inevitable probabilistic property [9]. In particular, to achieve higher single-photon purity, the HSPS system has to operate at low pumping power level, which limits the heralded single-photon (HSP) rate and hinders the practical application of HSPSs.

To break this trade-off between the HSP rate and the single-photon purity and to develop HSPSs toward a higher efficiency

and deterministic manner, one promising way is to multiplex a set of HSPSs (different modes) into one common output [8,10,11]. In such a multiplexing system, the detection of a heralding photon indicates the presence of a heralded photon at this certain mode. Many multiplexing schemes have been demonstrated, with modes in different degrees of freedom including space [12–17], time [17–20], frequency [21–23], and orbital angular momentum (OAM) [24]. Among these schemes, multiplexing HSPSs in the frequency domain (i.e., spectral multiplexing) attract great interest for their promising scalability as well as fixed losses and requirement of resources. There have been demonstrated spectral multiplexing HSPSs at wavelengths of ∼800 nm [21], 1.3 μm [22], and 1.5 μm [23]. For the out-of-the-lab application of long-distance quantum network, e.g., metropolitan quantum teleportation [25,26] and quantum key distribution (QKD) [27,28], single photons at 1.5 μm are preferred since they are within the lowest transmission window of optical fiber and many resources such as dense wavelength-division multiplexers (DWDMs) and potential quantum memory can be utilized [29]. Moreover, an HSPS with all the components integrated on a photonics chip has not yet been demonstrated, much less a multiplexing HSPS. In this regard, a fully on-chip multiplexing HSPS at 1.5 μm is particularly demanded.

In this paper, we propose a chip-scale HSPS on lithium niobate on insulator (LNOI) at 1.5 μm telecom-band based on spectral multiplexing and feed-forward control, as well as demonstrate a proof-of-principle experiment with discrete fiber-based components. In our proposal, all of the integrated components and those couplings among them can be realized by readily available technologies in LNOI-based integrated photonics. In the proof-of-principle demonstration, broadband correlated photon pairs are generated by the cascaded second-order harmonics generation (SHG) and SPDC processes in an integrated periodically poled lithium niobate (PPLN) waveguide module [30]. Three spectral modes within the idler spectrum are defined as the heralding spectral modes while different active feed-forward spectral manipulations are applied on the signal photon side when a corresponding heralding photon is detected in a spectral mode-resolved way. Our experimental results show a breakthrough of trade-off between the HSP rate and the single-photon purity. With continuous-wave (CW) laser pumping and three modes multiplexed, the measured HSP rate is enhanced by near threefold toward 3.1 kHz at low pumping power level while keeping an ultra-low $g^{(2)}(0)$ value of $0.0006 \pm 0.0001$. The heralded single photons reach a $g^{(2)}(0)$ as low as $0.0140 \pm 0.0009$ with a measured HSP rate of 21.2 kHz. The measurement of joint spectrum intensity (JSI) reveals that the spectral manipulation at single-photon level brings photons from three spectral modes to the common spectral mode. For the first time, we investigate the Hong–Ou–Mandel (HOM) interference between the spectrally multiplexed HSPS and an independent weak coherence source and achieve an HOM effect with a visibility of $60.99\% \pm 4.80\%$, indicating that the indistinguishability of the multiplexed HSPs is higher than 90%. This high indistinguishability shows great potential application in quantum teleportation [25,26], measurement-device-independent (MDI) QKD [31], and linear optical quantum computing [32]. Overall proof-of-principle results show the feasibility of our proposed chip-scale platform and great potential for future on-chip spectrally multiplexed HSPS using readily available technologies of LNOI-based integrated photonics.

## 2. PRINCIPLES AND RESULTS

### A. Principle of Future On-Chip Spectrally Multiplexed Single-Photon Source

Crystalline lithium niobate has been widely used in research of optical quantum technologies for its high non-linearity, high electro-optic coefficients, and broadband transmission window [33]. In recent years, the development and commercialization of technologies in manufacturing and fabricating LNOI has made this platform a promising candidate in realizing complex quantum photonic circuit [34,35]. Here, we propose an integrated scheme of spectrally multiplexed HSPS based on an LNOI platform, which includes a pump laser module, photon-pair generation module, filtering and photon detecting module, and feed-forward and frequency shifting module, as illustrated in Fig. 1(a). In particular, the pump laser module injects light at 1.5 μm into the photon-pair generation module to induce non-linear processes. The pump laser module can be an InP laser transferred and placed onto an unpatterned insulator layer, which can be realized by pick-and-place tools [36,37]. The photon-pairs generation module includes a PPLN waveguide on LNOI [38–40] in which enhanced cascaded SHG and SPDC [41,42] processes occur and then correlated photon pairs are generated, as shown in Fig. 1(b). Photonic wire bonding can be used for low-loss coupling from the pump laser to the PPLN waveguide [43–45]. This method can also be employed to couple the generated signal and idler photons into the following filtering and photon detecting module. In the filtering and photon detecting module, signal photons in a certain frequency band are selected by a demultiplexer and then delayed by a section of on-chip delay line, while their idler twins are selected with finer frequency grids and finally coupled into on-chip superconducting nanowire single-photon detectors (SNSPDs). The on-chip demultiplexer can be realized by arrayed waveguide gratings [46–48] or cascaded Mach–Zehnder interferometers [49] on LNOI. The optical true delay lines on LNOI with low propagation losses [50] and LNOI waveguide-integrated SNSPDs [51,52] required in the filtering and photon detecting module are both in the reach of recent technology. Detection events of idler photons generate heralding electronic signals, which are then sent to an integrated logic circuit in the feed-forward and frequency shifting module via bonded wires [53]. At the same time, the signal photons are coupled into an electro-optic phase modulator (EOM) on LNOI [54–56]. Driven by the frequency shifting signals output from the integrated logic circuit, the EOM converts the frequency of signal photons from different spectral modes, as shown in Fig. 1(c). Detection events of idler photons from different frequency channels lead to electronic signals with different magnitudes of frequency shifting for signal photons, which guarantees that all the signal photons are finally converted into a common spectral mode. After the frequency

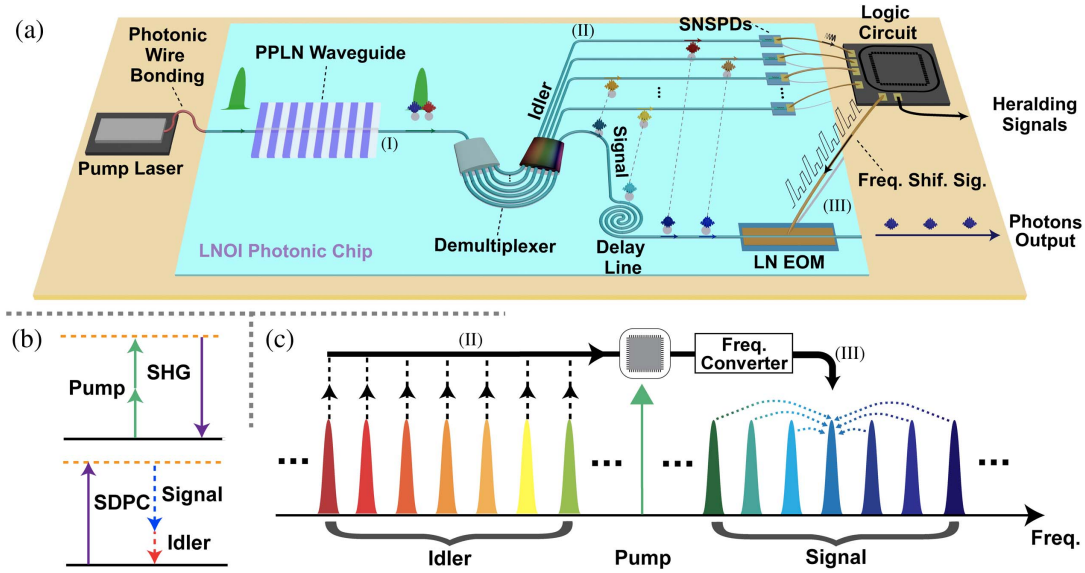


**Fig. 1.** Principles of chip-scale LNOI-based spectrally multiplexed HSPS. (a) A view of future chip-scale LNOI-based spectrally multiplexed HSPS, in which all basic components are integrated on an LNOI photonic chip including pump laser module, (I) photon-pairs generation module, (II) filtering and detecting module, and (III) feed-forward and frequency shifting module. (b) Energy conservation graph of SHG and SPDC. (c) Illustration of multiplexing in frequency domain. Photon-pairs generation module (I) generates broadband correlated signal and idler photons through cascaded SHG and SPDC processes. Idler photons are filtered into different spectral modes and detected by SNSPDs in the filtering and detecting module (II). Detection signals are sent to the logic circuit. The logic circuit sends frequency shifting signal to the feed-forward and frequency shifting module (III), where signal photons are shifted into the common spectral mode. LNOI, lithium niobate on insulator; PPLN, periodically poled lithium niobate; LN, lithium niobate; EOM, electro-optic phase modulator; SNSPD, superconducting nanowire single-photon detector; Freq. Shif. Sig., frequency shifting signals; SHG, second-order harmonics generation; SPDC, spontaneous parametric downconversion.

shifting operation, the signal photons are coupled out for applications.

### B. Proof-of-Principle Experimental Setup

The viability of the concept illustrated in Fig. 1 is demonstrated in a proof-of-principle experiment with discrete fiber-based components. Figure 2 shows the experimental setup. In this scheme, broadband photon pairs are generated by cascaded SHG and Type-0 SPDC processes in a fiber-connected PPLN waveguide. Under this configuration of non-linear processes, the wavelengths of pumping photons, signal photons, and heralding photons are all at 1.5 μm telecom-band, which is compatible with optical fiber telecommunication systems. After

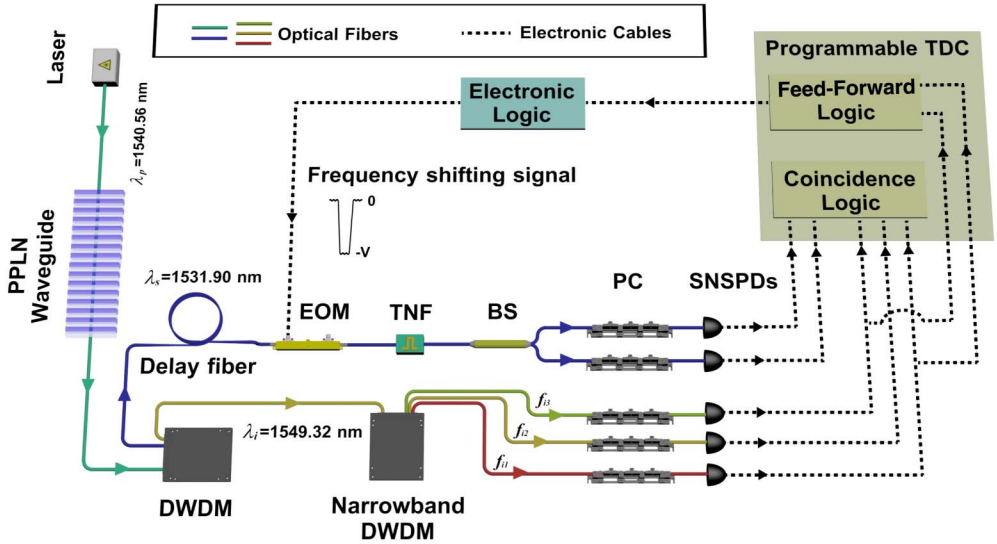


**Fig. 2.** Experimental setup for spectrally multiplexed HSPS. PPLN, periodically poled lithium niobate; DWDM, dense wavelength-divided multiplexer; EOM, electro-optic phase modulator; TNF, tunable narrowband filter; BS, beam splitter; PC, polarization controller; TDC, time-to-digit convertor; SNSPD, superconducting nanowire single-photon detector.

exiting from the PPLN waveguide, correlated signal photons and heralding photons with a bandwidth of ~100 GHz are selected and separated by DWDM. Heralding photons with three spectral modes, labeled by their central frequencies $f_{i1}$, $f_{i2}$, and $f_{i3}$, respectively, are further filtered out by using a fiber-based narrowband DWDM with channel spacing of 12.5 GHz and transmission bandwidth of 6.5 GHz for each channel. Here, $f_{i1} = 193.4992$ THz (1549.36 nm), $f_{i2} = 193.5117$ THz (1549.26 nm), and $f_{i3} = 193.5242$ THz (1549.16 nm). These three frequencies are defined as the heralding modes. Heralding photons from each mode are individually detected by three SNSPDs. Detection events of those $f_{i1}$ or $f_{i3}$ photons are sent to the feed-forward logic where each detection event triggers the logic circuit, driving electronic devices to fire a corresponding frequency shifting signal toward the EOM. For signal photons, before arriving at the EOM, they are delayed by a fiber loop so as to match the timing sequence with the electronic frequency shifting signal generated by their twins. By doing so, signal photons get frequency shifted and are multiplexed into a common spectral mode (see Appendix A for details).

We verify the spectral property of the heralded signal photons with and without applying the frequency shifting signal, respectively. Here, signal photons are selected in the frequency domain by varying the filtering window of a tunable narrowband filter (TNF) which has a bandwidth of 12.5 GHz. The coincidence events between signal photons and heralding photons are counted by the coincidence logic circuit. The results are shown in Fig. 3. In Fig. 3(a), without applying frequency shifting, it is obvious that the spectra of signal photons are separated into three spectral modes, $f_{s+}$, $f_{s0}$, and $f_{s-}$, corresponding to those heralding photons with the same mode spacing following the energy conservation. Here, $f_{s+} = 195.7006$ THz (1531.93 nm), $f_{s0} = 195.6881$ THz (1532.03 nm), and $f_{s-} = 195.6756$ THz (1532.13 nm). As frequency shifting signal is applied, photons in those spectral modes $f_{s+}$ and $f_{s-}$ get frequency shifted and indistinguishably moved into the $f_{s0}$ mode, as shown in Fig. 3(b). We realize the symmetric frequency up- and down-shifting with an efficiency higher than 90% (see Appendix B for details). It is worth noting that compared with the frequency shifting scheme of Bragg scattering four-wave mixing [22], the EOM-based frequency shifting scheme is less impacted by noise photon and has more advantage for integration [54].

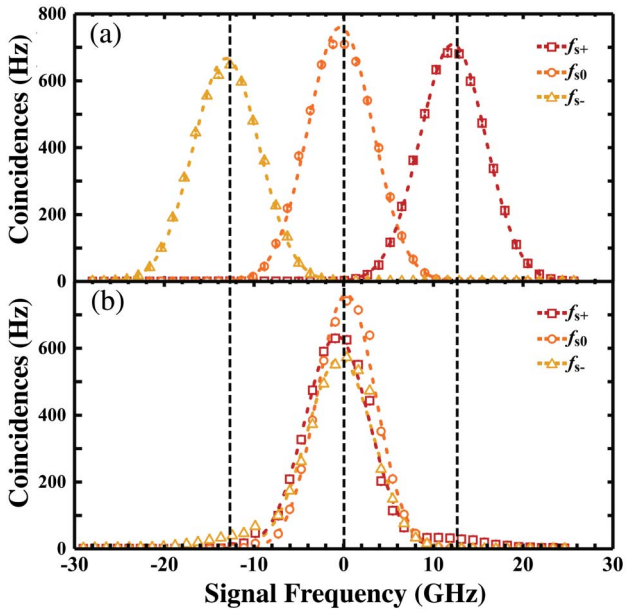


**Fig. 3.** Coincidence count rates without and with frequency shifting. (a) and (b) are the measured coincidence count rates among three individual spectral modes without and with spectral multiplexing, respectively, under the CW pumping power of 4 mW. The horizontal axis corresponds to the relative frequency difference with respect to $f_{s0}$. Red rectangles, orange circles, and yellow triangles represent the coincidence count rate of single photons to heralding photons at spectral modes $f_{s+}$, $f_{s0}$, and $f_{s-}$, respectively. Dashed curves are fitted by Gaussian functions which describe the frequency response of individual channels from the narrowband DWDM.

### C. Brightness and Coincidences-to-Accidentals Ratio

We characterize the source brightness, i.e., HSP rate, with experimental setup running in both multiplexing enabled and disabled cases, when CW lasers with different pump powers are applied, as shown in Fig. 4(a). Here, the HSP rate is defined as the coincidence count rate measured in the experiment without the correction for detector efficiency. The multiplexed HSP rate is measured by fixing the TNF at the center frequency of $f_{s0}$ with multiplexing enabled, while the HSP rates of three individual spectral modes are measured by fixing the center frequency of the TNF at $f_{s+}$, $f_{s0}$, and $f_{s-}$, respectively, with multiplexing disabled.

In Fig. 4(a), it can be seen that the multiplexed source has an HSP rate enhanced by a factor of $2.80 \pm 0.12$ compared with non-multiplexed individual modes in the low pumping power region (less than 4 mW in our experiment). The enhancement, drawing down as pumping power increases, is intrinsically hindered by the imperfect frequency response of electronic devices. Due to this non-ideal frequency response, some frequency shifting signals are lost in the high pumping power region (see Appendix B). Under the pump power of 16.98 mW, the multiplexed HSPS reaches the highest HSP rate of 23.6 kHz.

The coincidences-to-accidentals ratio (CAR) is a powerful tool to estimate how many undesired noise photons are generated together with the genuine correlated photon pairs. It can be defined as the ratio of the coincidence count rate between signal and heralding photons to the accidental count rate. We measure the CAR versus HSP rate for the multiplexed source and three individual modes. As shown in Fig. 4(b), the CAR of the multiplexed source is higher than those of individual modes. The CAR decreases at a higher HSP rate, since the main source of noise is Raman scattering photons and multipair events [30]. In our demonstration, a high-performance multiplexing HSPS is obtained with the CAR higher than 2000 at the HSP rate of 4 kHz. This value of multiplexed HSP rate also shows an enhancement of $2.80 \pm 0.12$ when compared with HSP rates of individual modes without multiplexing at the same CAR value. Though such enhancement would be deteriorated by the imperfect frequency response of electronic devices at a high HSP rate, a CAR higher than 100 can still be obtained.

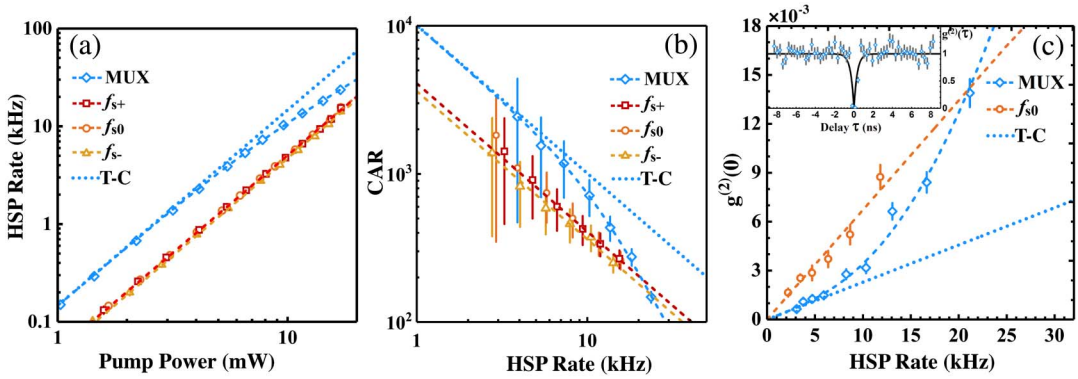


**Fig. 4.** Experimental results from multiplexing of three spectral modes. Blue diamonds are multiplexed source, and red rectangles, orange circles, and yellow triangles represent individual spectral modes of $f_{s+}$, $f_{s0}$, and $f_{s-}$, respectively. Dashed curves are fitted according to the theory model of our experiment. Dotted line is the theoretical calculation under the condition of perfect frequency response of electronic devices. (a) HSP rate versus pump power. The HSP rate of the multiplexed source is 2.80 ± 0.12 times larger than that of individual spectral modes at low pump power. The multiplexed HSP rate reaches 23.6 kHz under the pumping power of 16.98 mW. (b) CAR versus HSP rate. The CAR of the multiplexed source shows an improved performance than that of individual HSPS under fixed HSP rate. At low count rate, the multiplexed source has a CAR exceeding 2000 along with 2.80 ± 0.12 times enhancement while remains high at 100 for large HSP rates. (c) $g^{(2)}(0)$ versus HSP rate. We select the spectral mode $f_{s0}$ as a contrast to its multiplexed counterpart. It shows that the $g^{(2)}(0)$ of the individual source increases nearly 3 times rapider than the multiplexed one in the low HSP rate region as well as theoretically. Inset: heralded single-photon autocorrelation at an HSP rate of 21.1 kHz. The black curve represents the $g^{(2)}(\tau)$ fitting. The antibunching dip is at 0.0140 ± 0.0009. MUX, spectral multiplexing; T-C, theoretical calculation; HPS, heralded photon rate. Error bars are estimated using Poisson statistics.

### D. Single-Photon Purity

We obtain the single-photon purity of our spectrally multiplexed HSPS by measuring the second-order autocorrelation function $g^{(2)}(\tau)$ through the Hanbury-Brown and Twiss setup [57]. For the case of HSPS, the second-order autocorrelation function can be express as

$$g^{(2)}(\tau) = \frac{C_{ABH}(\tau)H}{C_{AH}(\tau)C_{BH}(0)}, \quad (1)$$

where $C_{ABH}$ is the coincidence count of detection events from detectors $A$ and $B$ that are connected with two output ports of the beam splitter conditioned by the heralding signal (i.e., three-fold coincidence); $C_{AH}$ ($C_{BH}$) represents the coincidences between the detection events from detector $A$ ($B$) and the heralding signal; and $H$ is the individual count rate of heralding events. Here, $\tau$ is the electronic delay between the detection events from detector $A$ and detector $B$. A full description of $g^{(2)}(\tau)$ is shown in the inset of Fig. 4(c). The $g^{(2)}(\tau)$ at zero delay, i.e., $g^{(2)}(0)$, can effectively characterize the single-photon purity, and what Fig. 4(c) shows is the measured $g^{(2)}(0)$ under different HSP rates when multiplexing is enabled and disabled. With three spectral modes multiplexed, we obtain $g^{(2)}(0)$ as low as 0.0140 ± 0.0009 at the measured maximum HSP rate. Comparing the $g^{(2)}(0)$ results with multiplexing on and off in Fig. 4(c), we can conclude that when the system is operating at low power region, the $g^{(2)}(0)$ for the non-multiplexed HSPS can be reduced by nearly 3 times after the multiplexing is introduced. We obtain an ultra-low $g^{(2)}(0) = 0.0006 \pm 0.0001$ when the multiplexed HSP rate is 3.1 kHz, comparing with the non-multiplexed case at the same HSP rate with $g^{(2)}(0)$ near 0.0020. In the region of high HSP rate, such improvement gets weakened because of the limited frequency response of the electronic system for frequency shifting signal generation. If the electronic signal generation system is designed elaborately, the improvement in single-photon purity by multiplexing can be kept linear, even when the HSP rate is sufficiently high, as shown in the theoretically calculated curve in Fig. 4(c).

### E. Joint Spectral Intensity and Hong–Ou–Mandel Interference

We study the spectral property of our proposed multiplexed HSPS by analyzing the JSI of photon pairs as well as HOM interference between the multiplexed HSPS and a weak coherence single-photon source. The JSI is given by the mode square of joint spectral amplitude [58] which can be measured by signal–idler photon coincidences versus $f_s$ and $f_i$, i.e., the signal frequency and the idler frequency.

Pumping the PPLN waveguide in Fig. 2 with pulsed laser, we measure the JSI (see Appendix D). Figures 5(a)–5(c) show the JSIs of photon pairs directly output from PPLN without filtering, photon pairs with narrowband DWDM inserted into the idler arm when multiplexing is disabled, and photon pairs with multiplexing enabled. As shown in Fig. 5(a), for the broadband nature of the PPLN waveguide, the JSI exhibits a diagonal band with strong frequency correlation. The cross-sectional width $\delta f_p = 6.4$ GHz corresponds to the bandwidth of the pulsed pump. In Fig. 5(b), the JSI is broken into three circle-like islands, corresponding to the three heralding modes defined by the three transmission bands of the narrowband DWDM. Based on the measured JSI, we calculate the Schmidt number $K = 3.07$ [59], which is in accordance with the number of selected spectral modes. The intensity of spectral mode $f_{s+}$ is lower than that of the other two islands, since the loss of the corresponding idler channel is 1 dB higher than in the other two channels. As shown in Fig. 5(c), with the spectral multiplexing being turned on, the island with spectral mode $f_{s+}$ ($f_{s-}$) moves downwards (upwards) and all of the three

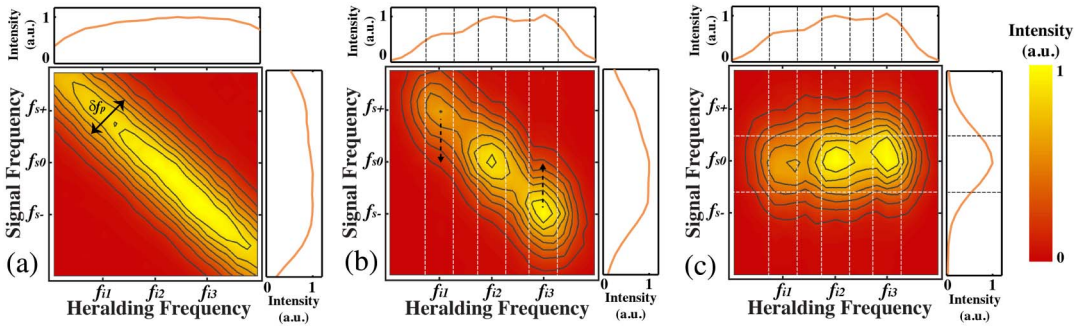


**Fig. 5.** Joint spectrum intensity (JSI) between heralding and signal photons in the $f_s - f_i$ plane. Three JSIs shown here are measured by placing two TNFs in the signal arm and heralding arm, respectively, and counting the coincidences by sweeping frequencies of $f_s$ and $f_i$. The top and right graphs for each JSI represent the marginal intensity distribution of the heralding and signal sides, respectively. The vertical and horizontal white (black) dashed lines depict the bandwidth of filters for the heralding and signal arms, respectively. Here, $f_{i1} = 193.4992$ THz (1549.36 nm), $f_{i2} = 193.5117$ THz (1549.26 nm), and $f_{i3} = 193.5242$ THz (1549.16 nm) while $f_{s+} = 195.7006$ THz (1531.93 nm), $f_{s0} = 195.6881$ THz (1532.03 nm), and $f_{s-} = 195.6756$ THz (1532.13 nm). (a) Photon pairs directly out of the PPLN waveguide without filtering. The diagonal band exhibits a high frequency correlation. (b) Photon pairs with narrowband DWDM applied in the heralding arm when multiplexing disabled. The JSI is broken into islands with three spectral modes corresponding to the narrowband DWDM. The circle-like island from each spectral mode exhibits a good spectral purity. Note that spectral mode $f_{s+}$ has an additional 1 dB loss from the idler arm. (c) Photon pairs with multiplexing enabled. The islands of spectral modes $f_{s+}$ and $f_{s-}$ are shifted into the central spectral mode.

islands enter into a common horizontal band. Within this band, the information of idler frequency is unable to give any information about the signal frequency. This means that the multiplexed photon pairs are spectrally uncorrelated. A spectral purity of 0.80 is calculated based on the measured JSI [59]. With a narrower filter applied, the spectral purity of multiplexed single photons will be further improved.

To further characterize the non-classical nature and indistinguishability of our spectrally multiplexed HSPS, we demonstrate an experiment of HOM interference between the multiplexed HSPS and an independent weak coherence single-photon source. HOM interference from independent sources is very important in many applications such as quantum teleportation [25,26] and MDI-QKD [31]. For general photon-pair sources, the individual signal mode or heralding mode does not deliver a non-classical photon-number statistics unless extracting the single photon nature by the heralding procedure [60]. Visibility higher than 50% is used as a criterion to determine whether the non-classicality takes place in HOM interference between photons from independent sources [61]. The weak coherence source not only serves as the quasi-single-photon source for the HOM effect from independent sources, but also, this kind of interference between single photons and photons from a weak coherence source can be used in some areas such as homodyne detection [62] and quantum circuits [63]. Here, the HOM interference experiment is carried out by launching balanced field intensity into two input ports, meaning that the mean photon numbers are equal when two input fields are respectively launched into two input ports of the beam splitter. As shown in Fig. 6, the visibility of twofold coincidences without the heralding procedure is $39.85\% \pm 1.63\%$ while the visibility after the heralding procedure (i.e., threefold coincidences) reaches $60.99\% \pm 4.80\%$ without subtracting the contribution of accidental events, indicating a non-classical nature. The threefold coincidences are post-selected by the heralded signal with the spectral purity imperfection taken into account. According to our theoretical calculation of the HOM interference between independent sources, the theoretical upper bound of the visibility should be 66.67% when the spectrally pure single photons interfere with photons from a weak coherence source at the same mean photon number [64,65] (see Appendix E). The genuine threefold visibility of this HOM interference between the multiplexed

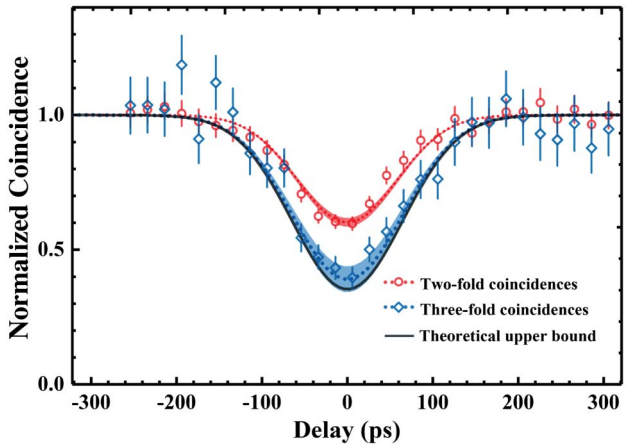


**Fig. 6.** HOM interference between the multiplexed source and the weak coherence source. Red circles are twofold coincidences measured without the heralding procedure. Blue diamonds are threefold coincidences measured under the condition by the heralding procedure without subtracting the contribution of the multiphoton event. Both twofold and threefold coincidences are fitted by Gaussian functions with red and blue curves and have the visibility of $39.85\% \pm 1.63\%$ and $60.99\% \pm 4.80\%$, respectively. Both twofold and threefold visibilities are 1000-time Gaussian fitting results with the Monte Carlo method. The red and blue bands represent the fitting variances of twofold and threefold HOM effects, respectively. The black solid curve represents the theoretically calculated upper bound of the threefold HOM interference at 66.67%. Error bars are estimated using Poisson statistics.

HSPS and weak coherence source approximates the upper bound of 66.67%, indicating highly indistinguishable photons emitted from the multiplexed single-photon source. If replacing the weak coherence source by a genuine single-photon source, based on our theoretical model, the visibility of HOM interference is expected to be 91.5%, which is close to unity. The small degrade of visibility from unity is mainly contributed by the noise of the detectors as well as residual multiphoton generation events in our spectrally multiplexed HSPS.

## 3. DISCUSSION AND CONCLUSION

In this paper, we propose a chip-scale LNOI-based spectral multiplexing HSPS at telecom-band and demonstrate a proof-of-principle experiment, yielding a significantly enhanced performance using discrete fiber-based components. The enhancement is possible to behave as our theoretical model and perfectly close to the number of multiplexing modes when the faster electronic devices are utilized. Furthermore, the first implementation of HOM interference from independent sources between our multiplexed source and a weak coherence single-photon source shows the evidence of non-classical nature. The results show the viability that large-scale integration of photonic chip HSPS has great potential in realizing a high-performance single-photon source.

In our demonstration, we use a tunable filter as the output filter for HSPS and a fiber-based EOM for frequency shifting, which both introduce relatively high loss. These losses, as well as losses from other fiber-based components, will degrade the photons collection efficiency and heralding efficiency (see details in Appendix F). The use of an integrated platform (see Fig. 1) will address the problem of component and connection losses as well as improve the performance of HSPS significantly.

Furthermore, scalable multiplexing is promising in our proposed integrated scheme if a larger magnitude of frequency shifting is applied. The recently developed integrated lithium niobate EOM has low $\pi$-voltage at $V_\pi = 1.4$ V and ultra-low loss at ~0.5 dB [54], which is possible to reach a larger frequency shifting as well as better brightness and efficiency in spectrally multiplexed HSPS. Another possible way to enlarge the magnitude of frequency shifting is to use an arbitrary waveform generator (AWG) with faster sample rate. In this case, using the same way to prepare frequency shifting signals as we implemented (multiple high-voltage ramps with different amplitudes generated from the programmable AWG), the largest magnitude of frequency shifting can reach $\Delta f \approx 100$ GHz (see Appendix C). Hence, considering a spectral mode spacing of 12.5 GHz in our implementation, up to 17 spectral modes can be multiplexed (i.e., an enhancement of 12.3 dB) while consuming a bandwidth resource of only 200 GHz, which shows a good scalability. In our experiment, though, we define the enhancement of multiplexing without considering the loss of frequency converter (i.e., the EOM). Our proposed on-chip system with full capability of frequency shifting magnitude would yield a net enhancement factor of 11.8 dB (i.e., after subtracting the loss of the on-chip EOM) (see Appendix C).

We note that a related result of spectrally multiplexed HSPS at 1.5 μm has been implemented by Hiemstra *et al.* [23]. In their scheme, the EOM is also employed as the frequency converter, and the spectral mode resolving detection of heralding photons is realized by a time-of-flight spectrometer while applying the linear range of sinusoidal signal for frequency shifting. In comparison, our scheme utilizes voltage ramp as the frequency shifting signal (see Appendix C), which suffers less impact from the jitter of SNSPDs and timing electronics, providing a more precise active feed-forward control. Moreover, the magnitudes of voltage ramps are programmable and it is possible to include more voltage ramps with different magnitudes in multiplexing more spectral modes. We summarize recent demonstrated works of single-photon sources as well as their performance, as Table 1 shows. It is obvious that quantum-dot-based devices in a cryogenic environment can generate single photons with high rate and high single-photon purity, either in 700 nm, 900 nm, or 1.5 μm wavelength bands.

**Table 1. Summary of Single-Photon Source (SPS) Performance among Previous Demonstrations[a]**

| Year | Types of SPS | MUX DOF | $\lambda$ (nm) | Modes Num. | Temp. | $g^{(2)}(0)$ | Rate (kHz) | EF | Refs. |
|---|---|---|---|---|---|---|---|---|---|
| 2016 | HSPS | Space | 1550 | 2 | RT | 0.05 | 0.5 | 1.75 | [16] |
| 2016 | HSPS | Time | 1545 | 4 | RT | – | 0.6 | 2 | [19] |
| 2016 | HSPS | Space & Time | 1547 | 8 | RT | – | 0.3 | 2.14 | [17] |
| 2016 | QD | – | ~1550 | – | 8 K | 0.00044 | 196 | – | [66] |
| 2016 | QD | – | ~1550 | – | 80 K | 0.34 | – | – | [67] |
| 2017 | HSPS | Freq. | 795 | 3 | RT | 0.06 | 0.3 | ~1 | [21] |
| 2018 | HSPS | Freq. | 1280 | 3 | RT | 0.07 | 23 | 2.2 | [22] |
| 2018 | QD | – | ~790 | – | 4 K | 0.000075 | 60 | – | [68] |
| 2019 | HSPS | OAM | 1550 | 3 | RT | 0.048 | ~4.2 | 1.47 | [24] |
| 2019 | HSPS | Time | 1590 | 40 | RT | 0.007 | 25.5 | 27.9 | [20] |
| | | | | | | 0.088 | 206 | 18.7 | |
| | | | | | | 0.269 | 334 | 9.7 | |
| 2019 | QD | – | ~890 | – | 1.5 K | 0.025 | 13700 | – | [69] |
| 2020 | HSPS | Freq. | 1565 | ~3 | RT | ~0.15 | ~12 | 2.7 | [23] |
| | | | | | | ~0.01 | ~0.8 | 2.7 | |
| **2021** | **HSPS** | **Freq.** | **1532** | **3** | **RT** | **0.0006** | **3.1** | **2.8** | **This work** |
| | | | | | | **0.014** | **21.1** | **~1.2** | |

[a]MUX, multiplexing; DOF, degree of freedom; Temp., temperature; EF, enhancement factor; RT, room temperature; QD, quantum dot; Freq., frequency. The rate in the table refers to the measured rate of coincidence in the experiment.

However, in some cost-sensitive applications for quantum networks [25,26,70], high-performance 1.5 μm single-photon sources working at ambient temperatures are preferred. We highlight that our spectrally multiplexed HSPS is working at room temperature and has an ultra-high single-photon purity with $g^{(2)}(0) = 0.0006 \pm 0.0001$ at an HSP rate of 3.1 kHz, which means a near-ideal single-photon purity ever reported. This record-high performance of spectrally multiplexed single-photon source (in terms of $g^{(2)}(0)$ and single-photon rate) has great advantage in the applications of quantum communication. For example, it can dramatically reduce the bit error rate in quantum teleportation and QKD. Our spectrally multiplexed HSPS also shows a high indistinguishability (an HOM visibility higher than 90%) especially after the spectral manipulation. The indistinguishability together with the property of ultra-high single-photon purity will benefit a lot to various of quantum applications, e.g., linear optical quantum computing with an unprecedented noise tolerance [32]. In summary, our proposal of on-chip scalable spectrally multiplexed HSPS and the results of the proof-of-principle demonstration are useful for developing a high-quality single-photon source.

## APPENDIX A: DETAILS OF THE EXPERIMENTAL SETUP

As described in the main text, the proof-of-principle demonstration of spectrally multiplexed HSPS in discrete fiber-based components is experimentally realized as follows. Spectral mode-resolved detection of heralding photons tells the feed-forward logic about the frequency information while the feed-forward logic then gives the frequency converter, i.e., electro-optic modulator, a corresponding frequency shifting signal. Finally signal photons are shifted into the central spectral mode. Here, the pumping field centered at $\lambda_p = 1540.16$ nm is sent into a PPLN waveguide, which generates broadband photon pairs with Type-0 phase matching condition. Note that both SHG and SPDC processes take place in the PPLN waveguide and both input and output ports of the PPLN waveguide are coupled with single-mode fibers. The generated photon pairs are separated into signal and heralding arms by a commercial DWDM with ∼100 GHz bandwidth centered at $\lambda_s = 1531.90$ nm and $\lambda_i = 1549.32$ nm, respectively. The idler arm is further filtered by a fiber-based narrowband DWDM (MICS, Kylia) with channel spacing of 12.5 GHz and the transmission bandwidth of each channel is 6.5 GHz. For the heralding and multiplexing procedures, those electronic signals, from the detection events of three different modes, $f_{i1}$, $f_{i2}$, and $f_{i3}$, are combined in the coincidence logic as heralding signals. At the same time, the detection events of $f_{i1}$ or $f_{i3}$ photons generate corresponding trigger signals to the feed-forward logic. Both the coincidence logic and feed-forward logic are realized by a programmable time-to-digit converter (TDC, ID900, ID Quantique Corp.). For signal photons, before arriving at the EOM for spectral multiplexing, they are delayed by a 250 m fiber to match the timing sequence with the electronic frequency shifting signal generated by their twins. The reason for adding a 250 m long delay fiber is mainly because the AWG (Tektronix Corp., 70002A) is operating at triggering mode, in which this equipment has a minimum global delay at 1 μs. Also, there are several meters (∼30 m) of patch fibers and electronic cables on the pathway from the narrowband filtering of idler photons to the arrival of frequency shifting signals at the EOM. However, in our proposal of chip-scale spectrally multiplexed HSPS, all these time delays from the transmission of photons or electronic signals can be reduced into negligible with the help of integrated SNSPDs on waveguide, on-chip electronic wire bonding [53], as well as replacing the AWG with a miniature logic circuit [71]. Thus, in the on-chip scheme, the delay of signal photons overall needs the length of the on-chip delay line at <100 cm, which is feasible using current technology [50].

## APPENDIX B: FREQUENCY SHIFTING SIGNAL

In our demonstration of spectrally multiplexed HSPS, the frequency shifting signal is generated from a series of electronic devices; see Fig. 7(a). The AWG operating at trigger mode at a sampling rate of 25 GSa/s, is triggered by signals that come from the feed-forward logic, producing a pre-programmed pulse signal with ultra-fast pulse edge. Both a high-speed amplifier (S126A, SHF Communication Technologies AG) with 25 GHz bandwidth and a home-made high-voltage radio frequency (RF) transistor are used to amplify the pulse signal. The AWG signal is first amplified by the high-speed amplifier, and

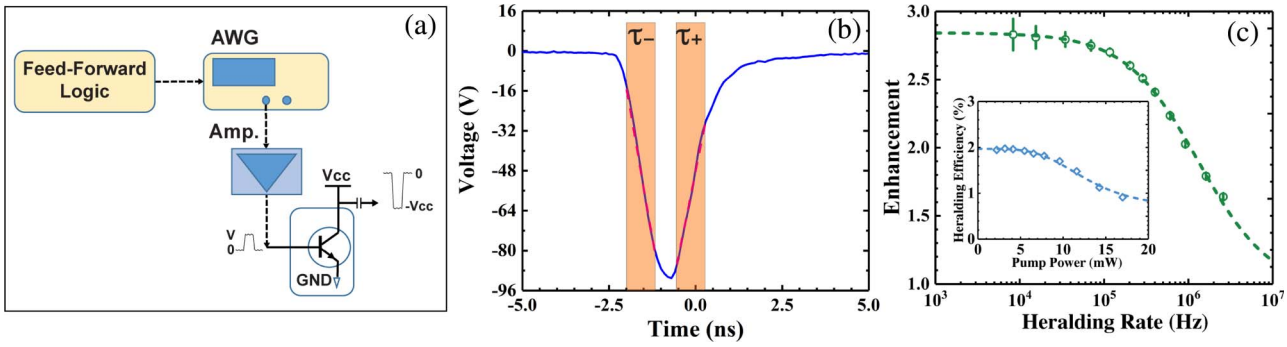


**Fig. 7.** (a) Experimental setup for generation of frequency shifting signals. AWG, arbitrary waveform generator; Amp., microwave amplifier. (b) Typical electronic signal for frequency shifting. (c) Enhancement of the multiplexed source versus heralding rate. Inset: Heralding efficiency of the multiplexed source versus pump power. Green circles and blue diamonds are measured data while green and blue dashed curves are the result of theoretical calculation. Error bars are estimated using Poisson statistics.

then triggers the RF transistor to fire a reversed pulse with linear high-voltage ramp, where the rising edge $\kappa_+$ and the falling edge $\kappa_-$ are nearly symmetric. Here, $\kappa_\pm$ represents the voltage ramp of the pulse edge; see Fig. 7(b). The pulse is further sent to the EOM (CETC Corp.), driving the EOM to modulate the phase of the single-photon wave packet as follows [21]:

$$\varepsilon(x,t) = |\varepsilon(x,t)| \exp\left[i2\pi\left(f_0 + \frac{\kappa_\pm}{2V_\pi}\right)t - ikx\right], \quad \textbf{(B1)}$$

where the single-photon wave packet $\varepsilon(x,t)$ is depicted by the slowly varying envelope approximation while $V_\pi$ is the $\pi$-voltage of the EOM. The linearly varying time-dependent change in the phase of the photon yields a frequency shifting with the shifting magnitude of $\Delta f = \kappa_\pm/2V_\pi$. Here, the ultra-fast pulse edge $\kappa_+$ ($\kappa_-$) leads to frequency upconversion (downconversion). To realize precise frequency shifting, the trigger signals generated by detection events of $f_{i1}$ and $f_{i3}$ photons are combined by the feed-forward logic, where a certain electronic delay is added to the $f_{i1}$ signals to compensate the time difference between pulse edges $\kappa_+$ and $\kappa_-$ in the same pulse.

The enhancement versus heralding rate of the multiplexed source system is shown in Fig. 7(c). The deterioration of enhancement is mainly contributed by the poor frequency response of the AWG. Here, the AWG runs in trigger mode in which each input signal that comes from the feed-forward logic triggers the generation of a corresponding pulse from the AWG. The trigger mode of the AWG has a low-pass frequency response which we model as a low-order Butterworth filter with a 3 dB bandwidth of 1.2 MHz. The feed-forward signal and therefore the frequency shifting signal have a higher possibility to lose under a higher heralding rate. In this way, $f_{s+}$ and $f_{s-}$ photons have less possibility to be shifted into the center spectral mode and ultimately degrade the enhancement of the multiplexed source. Similarly, the heralding efficiency is also affected by this mechanism as the inset of Fig. 7(c) shows. The data points are in agreement with the theoretical prediction. Here, we note that the degradation of enhancement is only affected by the inner mechanism of the AWG. Using currently off-the-shelf electronic devices, the performance of our multiplexed source will follow the theoretical calculation curve (see Fig. 3). Moreover, in the on-chip LNOI-based HSPS proposal, the AWG can be replaced by a compact ultra-narrow pulse generator [71,72], in which higher voltage ramps can be generated from this miniaturized module.

## APPENDIX C: SCALABLE MULTIPLEXING

The currently available AWG with 100 GSa/s sampling rate shows a fourfold improvement compared with our scheme, while the $\pi$-voltage of the on-chip EOM [54] is nearly half comparing with the fiber-based EOM. In this case, using the same way to prepare frequency shifting signals as we implemented, the largest magnitude of frequency shifting can reach $\Delta f \approx 4 \times 2 \times 12.5$ GHz $= 100$ GHz. For a larger number (e.g., $N$) of multiplexing, the frequency shifting signal will include $N-1$ voltage ramps that correspond to $N-1$ magnitudes of frequency shifting. For example, in the case of the multiplexing scheme of 17 modes, the frequency shifting signal will have 16 voltage ramps with the magnitude of frequency shifting ranging from −100 GHz to 100 GHz with 12.5 GHz spacing. In our demonstration, the use of a programmable AWG makes it possible to generate arbitrary magnitudes of frequency shifting signals and finally realizes the large-scale multiplexing.

To get a net enhancement after spectral multiplexing, the loss of heralded photons introduced by frequency shifting devices should be compensated by the multiplexing. In detail, before multiplexing, the probability for a click on detector of heralded photons per pulse is [8]

$$\begin{aligned} P_{s1} &= \eta_s(1-\lambda^2)\sum_{n=0}^{\infty}[1-(1-\eta_i)^n]\lambda^{2n} \\ &\approx \eta_s\eta_i\lambda^2 + \eta_s(2\eta_i - \eta_i^2)\lambda^4, \end{aligned} \quad \textbf{(C1)}$$

where $\eta_{s,i}$ represents the collection efficiency of signal and heralding photons, while $\lambda \ll 1$ is a parameter related to the parametric gain in the SPDC process. After multiplexing, this probability turns to [8]

$$P_{s2} = \eta_s\eta_a[1-(1-P_{s1}/\eta_s)^N], \quad \textbf{(C2)}$$

where $N$ is the number of multiplexed modes, while $\eta_a$ represents the additional loss introduced by the frequency shifting devices. With the approximation

$$(1-P_{s1}/\eta_s)^N = \sum_{k=0}^{N} C_N^k(-P_{s1}/\eta_s)^k \approx 1 - NP_{s1}/\eta_s \quad \textbf{(C3)}$$

adopted, Eq. (C2) can be simplified into

$$P_{s2} \approx \eta_a N P_{s1}. \quad \textbf{(C4)}$$

For space or time multiplexing systems, the additional system loss $\eta_a$ increases when scaling up the multiplexing modes [8,22]. However, the $\eta_a$ is fixed for the spectral multiplexing system, and it is obvious that $\eta_a N$ is exactly the net enhancement factor for the spectral multiplexing system. With the near-term parameters mentioned above, we have $N = 12.3$ dB and $\eta_a = 0.5$ dB, which yields a net enhancement factor of 11.8 dB.

## APPENDIX D: MEASUREMENT OF JOINT SPECTRAL INTENSITY AND HONG–OU–MANDEL INTERFERENCE

In the scheme of JSI measurement, we add another TNF (OTF-970, Santec) in the heralding arm before the narrowband DWDM (not shown in the main text Fig. 1). The pulse laser pump is prepared by an intensity modulator (CETC Corp.) that modulates the CW laser (PPCL550, PURE Photonics Corp.) with a programmed RF signal generated from an AWG at a sampling rate of 25 GSa/s, which has a ∼65 ps width and 500 MHz repetition rate. The peak power of this pulse laser is 25 mW. With two TNFs (12.5 GHz bandwidth) placing separately in both the heralding and signal arms, the coincidences are measured by swapping two TNFs' central wavelengths respectively from 193.4867 THz to 193.5367 THz for the heralding arm and from 195.6631 THz to 195.7131 THz for the signal arm with a step of 2.5 GHz.

The multiplexing HSPS and a weak coherence source are used to perform the HOM interference. The pulsed laser is synchronized with the photon-pair source with a pulse bandwidth of 6.4 GHz and a repetition rate of 500 MHz. The HOM effect only occurs when two input photons are indistinguishable. Thus, the wavelengths of the two sources are both centered at 1532.03 nm ($f_{s0}$) while the input photons are both aligned to the same polarization with the help of polarization controllers. The output ports of the beam splitter used in HOM interference are sent to two SNSPDs (P-CS-6, PHPTEC Corp.) while the detection signals are collected and analyzed by the coincidence logic. Except for feed-forward control, the heralding signals are also sent to the coincidence logic circuit. The heralding signal is a conditional trigger in threefold coincidences. The coincidence logic can simultaneously analyze the coincidence events of the two beam splitter output ports with and without the trigger of the heralding signal, and hence we can measure both twofold and threefold coincidences at the same time. Therefore, by varying the optical tunable delay line and hence changing the relative delay between the two sources, the HOM effect can be observed.

## APPENDIX E: VISIBILITY OF HONG–OU–MANDEL INTERFERENCE

To understand the result of Fig. 5 in the main text, we start with analyzing the ideal HOM effect from independent sources. First, let us consider the 50:50 beam splitter with two input ports and two output ports, where field operators for input ports are represented as $\hat{a}_1$, $\hat{a}_2$ while those for output ports are represented as $\hat{a}_3$, $\hat{a}_4$. We can express these four field operators as

$$\hat{a}_3 = (\hat{a}_1 + \hat{a}_2)/\sqrt{2}, \qquad \hat{a}_4 = (\hat{a}_1 - \hat{a}_2)/\sqrt{2}, \tag{E1}$$

which we can calculate the output coincidence probability by considering their input fields. Here, the output coincidence probability $P$ can be described as [61,73]

$$\begin{aligned} P &\propto \langle \hat{a}_3^\dagger(t)\hat{a}_4^\dagger(t')\hat{a}_4(t')\hat{a}_3(t)\rangle \\ &= \frac{1}{4}(\langle \hat{a}_1^\dagger(t)\hat{a}_1^\dagger(t')\hat{a}_1(t')\hat{a}_1(t)\rangle + \langle \hat{a}_2^\dagger(t)\hat{a}_2^\dagger(t')\hat{a}_2(t')\hat{a}_2(t)\rangle \\ &\quad + \langle \hat{a}_1^\dagger(t)\hat{a}_2^\dagger(t')\hat{a}_2(t')\hat{a}_1(t)\rangle + \langle \hat{a}_2^\dagger(t)\hat{a}_1^\dagger(t')\hat{a}_1(t')\hat{a}_2(t)\rangle \\ &\quad - \langle \hat{a}_2^\dagger(t)\hat{a}_1^\dagger(t')\hat{a}_2(t')\hat{a}_1(t)\rangle - \langle \hat{a}_1^\dagger(t)\hat{a}_2^\dagger(t')\hat{a}_1(t')\hat{a}_2(t)\rangle), \end{aligned} \tag{E2}$$

where in the right-hand side of the equation, the first two terms are the autocorrelation function for the two input fields while the third and fourth terms are the cross correlation between these two fields. And finally, the last two serve as interference terms which lead to the interference effect. We can further derive a simpler description from Eq. (E2) as follows:

$$P \propto \frac{1}{4}(g_1^{(2)}(0)\bar{n}_1^2 + g_2^{(2)}(0)\bar{n}_2^2 + 2\bar{n}_1\bar{n}_2 - 2\bar{n}_1\bar{n}_2 I_{12}), \tag{E3}$$

where $\bar{n}_1$ and $\bar{n}_2$ are the mean photon number for the input fields of port 1 and port 2, respectively, and $I_{12} = \langle \hat{a}_1^\dagger(t)\hat{a}_2^\dagger(t')\hat{a}_1(t')\hat{a}_2(t)\rangle/\bar{n}_1\bar{n}_2$ represents the interference factor which ranges from 0 to 1 and depends on the temporal overlap of the two input fields. When two input fields are completely overlapped, i.e., $t = t'$, the interference factor shows $I_{12} = 0$, which corresponds to the dip of the HOM effect. While two input fields are temporally separated, the interference factor becomes 1, i.e., $I_{12} = 1$, and hence corresponds to the wing.

Now, consider the input fields $\hat{a}_1$ and $\hat{a}_2$ are ideally a thermal field and a coherent field, respectively, as the twofold coincidence we demonstrate. We can derive the visibility of twofold coincidence from Eq. (E3):

$$V_{\text{two-fold}} = \frac{2}{2\frac{\bar{n}_1}{\bar{n}_2} + \frac{\bar{n}_2}{\bar{n}_1} + 2}. \tag{E4}$$

In our implementation we have balanced input fields, which means that the mean photon numbers for the two input fields are equal, i.e., $\bar{n}_1 = \bar{n}_2$. That leads to a theoretical upper bound of twofold visibility as $V_{\text{two-fold}} = 40\%$.

Next, we consider the input fields $\hat{a}_1$ and $\hat{a}_2$ are ideally a single-photon field and a coherent field, respectively, and hence the threefold coincidence can also be expressed as

$$V_{\text{three-fold}} = \frac{2}{\frac{\bar{n}_2}{\bar{n}_1} + 2}. \tag{E5}$$

Again, in a balanced input with $\bar{n}_1 = \bar{n}_2$, it can be obtained that a theoretical threefold visibility is upper bounded to $V_{\text{three-fold}} = 66.67\%$. Note that in the configuration of the coincidence logic, the single-photon coincidence events are post-selected by the heralding signal with the gate logic, in which the ratio of the mean photon number between both input fields remains intact.

In HOM interference, the premise for ideal non-classical interference is that the photon participating in the interference is spectrally pure. The imperfection of single-photon spectral purity should be taken into consideration when revealing the non-classical nature of the threefold coincidence. For the imperfect spectral purity, we should take into account the unwanted external broadening mechanism. In our experiment, the bandwidth of the Gaussian pumping pulses is 6.4 GHz. Considering the SHG process and heralding procedure, the heralded signal photons have a broadened external bandwidth

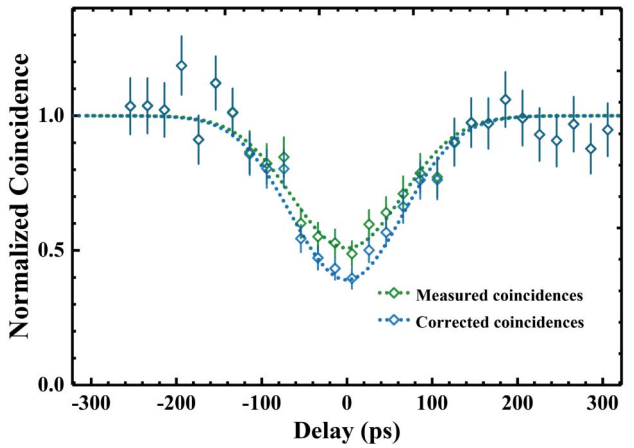


**Fig. 8.** Threefold coincidences before (green diamonds) and after (blue diamonds) correction. Error bars are estimated using Poisson statistics.

of 11.2 GHz, which is a convolution result of pump photon bandwidth and heralding photon bandwidth. Such mismatch between the internal and external bandwidth reduces the spectral purity of the single photon and shows an 81.16% deterioration of visibility [74], as Fig. 8 shows. This deterioration matches with the spectral purity at 0.80 calculated from the JSI after spectral multiplexing (see Fig. 6). This degrade can be further canceled by applying a narrower output filter for the HSPS. After correcting the spectral purity imperfection, the visibility of threefold coincidences ends up with 60.99% ± 3.50%.

## APPENDIX F: LOSSES AND EFFICIENCY

The implementation of the multiplexed HSPS has many fiber-based optical components, which introduce relatively large losses causing inefficient photon collection on both the heralding and heralded sides. We measure the overall component losses and efficiencies of the signal arm and heralding arm in three spectral modes, as shown in Tables 2 and 3. The total transmission efficiencies are the direct measurement of the component losses while the collection efficiencies are calculated by Klyshko method [75]. Here, the transmission efficiency in the signal arm is in accordance with its collection efficiency. The mismatch between transmission efficiency and collection efficiency in the heralding arm is because of the difference of filtering bandwidths between the signal and idler arms, which reduces the collection efficiency by a ratio of about 0.52. The residual small deviation might be attributed to the measurement error of component losses.

**Table 2. Overall Component Losses of the Signal and Heralding Arms[a]**

| Components | Losses (dB) |
|---|---|
| PPLN waveguide output coupling | 2.50 |
| DWDM-signal | 1.83 |
| DWDM-heralding | 2.21 |
| Narrowband DWDM-$f_{i1}$ | 4.58 |
| Narrowband DWDM-$f_{i2}$ | 4.58 |
| Narrowband DWDM-$f_{i3}$ | 4.60 |
| Delay fiber | 0.40 |
| EOM | 4.56 |
| TNF | 5.30 |
| SNSPDs | 1.80–2.20 |

[a]PPLN, periodically poled lithium niobate; DWDM, dense wavelength divided multiplexer; EOM, electro-optic phase modulator; TNF, tunable narrowband filter; SNSPD, superconducting nanowire single-photon detector.

**Table 3. Total Transmission Efficiencies and Collection Efficiencies of the Signal and Heralding Arms**

| Efficiencies | Value (%) |
|---|---|
| Transmission efficiency-signal arm | 2.10 |
| Transmission efficiency-heralding arm | 7.06 |
| Heralding efficiency | 2.15 |
| Collection efficiency-$f_{i1}$ | 5.34 |
| Collection efficiency-$f_{i2}$ | 4.87 |
| Collection efficiency-$f_{i3}$ | 5.43 |

**Funding.** Sichuan Province Science and Technology Support Program (2018JY0084); National Key Research and Development Program of China (2017YFA0304000, 2017YFB0405100, 2018YFA0306102, 2018YFA0307400, 2019YFB2203400); National Natural Science Foundation of China (12074058, 61405030, 61704164, 61775025, 62005039, 62075034, 91836102, U19A2076).

**Disclosures.** The authors declare that they have no competing interests.

**Data Availability.** Data underlying the results presented in this paper are not publicly available at this time but may be obtained from the authors upon reasonable request.

[†]These authors contributed equally to this paper.

## REFERENCES

1. C.-K. Hong, Z.-Y. Ou, and L. Mandel, "Measurement of subpicosecond time intervals between two photons by interference," Phys. Rev. Lett. **59**, 2044–2046 (1987).
2. Y.-H. Deng, H. Wang, X. Ding, Z.-C. Duan, J. Qin, M.-C. Chen, Y. He, Y.-M. He, J.-P. Li, Y.-H. Li, L.-C. Peng, E. S. Matekole, T. Byrnes, C. Schneider, M. Kamp, D.-W. Wang, J. P. Dowling, S. Höfling, C.-Y. Lu, M. O. Scully, and J.-W. Pan, "Quantum interference between light sources separated by 150 million kilometers," Phys. Rev. Lett. **123**, 080401 (2019).
3. N. Gisin, G. Ribordy, W. Tittel, and H. Zbinden, "Quantum cryptography," Rev. Mod. Opt. **74**, 145–195 (2002).
4. N. Gisin and R. Thew, "Quantum communication," Nat. Photonics **1**, 165–171 (2007).
5. J. L. O'brien, "Optical quantum computing," Science **318**, 1567–1570 (2007).
6. V. Giovannetti, S. Lloyd, and L. Maccone, "Quantum metrology," Phys. Rev. Lett. **96**, 010401 (2006).
7. I. Aharonovich, D. Englund, and M. Toth, "Solid-state single-photon emitters," Nat. Photonics **10**, 631–641 (2016).
8. E. Meyer-Scott, C. Silberhorn, and A. Migdall, "Single-photon sources: approaching the ideal through multiplexing," Rev. Sci. Instrum. **91**, 041101 (2020).
9. A. Christ and C. Silberhorn, "Limits on the deterministic creation of pure single-photon states using parametric down-conversion," Phys. Rev. A **85**, 023829 (2012).
10. A. L. Migdall, D. Branning, and S. Castelletto, "Tailoring single-photon and multiphoton probabilities of a single-photon on-demand source," Phys. Rev. A **66**, 053805 (2002).
11. T. Pittman, B. Jacobs, and J. Franson, "Single photons on pseudodemand from stored parametric down-conversion," Phys. Rev. A **66**, 042303 (2002).
12. X.-S. Ma, S. Zotter, J. Kofler, T. Jennewein, and A. Zeilinger, "Experimental generation of single photons via active multiplexing," Phys. Rev. A **83**, 043814 (2011).
13. M. J. Collins, C. Xiong, I. H. Rey, T. D. Vo, J. He, S. Shahnia, C. Reardon, T. F. Krauss, M. Steel, A. S. Clark, and B. Eggleton, "Integrated spatial multiplexing of heralded single-photon sources," Nat. Commun. **4**, 2582 (2013).
14. C. Xiong, T. D. Vo, M. Collins, J. Li, T. Krauss, M. Steel, A. Clark, and B. Eggleton, "Bidirectional multiplexing of heralded single photons from a silicon chip," Opt. Lett. **38**, 5176–5179 (2013).
15. T. Meany, L. A. Ngah, M. J. Collins, A. S. Clark, R. J. Williams, B. J. Eggleton, M. Steel, M. J. Withford, O. Alibart, and S. Tanzilli, "Hybrid photonic circuit for multiplexed heralded single photons," Laser Photonics Rev. **8**, L42–L46 (2014).
16. R. J. Francis-Jones, R. A. Hoggarth, and P. J. Mosley, "All-fiber multiplexed source of high-purity single photons," Optica **3**, 1270–1273 (2016).

17. G. J. Mendoza, R. Santagati, J. Munns, E. Hemsley, M. Piekarek, E. Martn-López, G. D. Marshall, D. Bonneau, M. G. Thompson, and J. L. O'Brien, "Active temporal and spatial multiplexing of photons," Optica **3**, 127–132 (2016).
18. F. Kaneda, B. G. Christensen, J. J. Wong, H. S. Park, K. T. McCusker, and P. G. Kwiat, "Time-multiplexed heralded single-photon source," Optica **2**, 1010–1013 (2015).
19. C. Xiong, X. Zhang, Z. Liu, M. J. Collins, A. Mahendra, L. Helt, M. J. Steel, D.-Y. Choi, C. Chae, P. Leong, and B. J. Eggleton, "Active temporal multiplexing of indistinguishable heralded single photons," Nat. Commun. **7**, 10853 (2016).
20. F. Kaneda and P. G. Kwiat, "High-efficiency single-photon generation via large-scale active time multiplexing," Sci. Adv. **5**, eaaw8586 (2019).
21. M. G. Puigibert, G. Aguilar, Q. Zhou, F. Marsili, M. Shaw, V. Verma, S. Nam, D. Oblak, and W. Tittel, "Heralded single photons based on spectral multiplexing and feed-forward control," Phys. Rev. Lett. **119**, 083601 (2017).
22. C. Joshi, A. Farsi, S. Clemmen, S. Ramelow, and A. L. Gaeta, "Frequency multiplexing for quasi-deterministic heralded single-photon sources," Nat. Commun. **9**, 847 (2018).
23. T. Hiemstra, T. Parker, P. Humphreys, J. Tiedau, M. Beck, M. Karpiński, B. Smith, A. Eckstein, W. Kolthammer, and I. Walmsley, "Pure single photons from scalable frequency multiplexing," Phys. Rev. Appl. **14**, 014052 (2020).
24. S.-L. Liu, Q. Zhou, Z.-Y. Zhou, S.-K. Liu, Y. Li, Y.-H. Li, C. Yang, Z.-H. Xu, G.-C. Guo, and B.-S. Shi, "Multiplexing heralded single photons in orbital-angular-momentum space," Phys. Rev. A **100**, 013833 (2019).
25. R. Valivarthi, Q. Zhou, G. H. Aguilar, V. B. Verma, F. Marsili, M. D. Shaw, S. W. Nam, D. Oblak, and W. Tittel, "Quantum teleportation across a metropolitan fibre network," Nat. Photonics **10**, 676–680 (2016).
26. Q.-C. Sun, Y.-L. Mao, S.-J. Chen, W. Zhang, Y.-F. Jiang, Y.-B. Zhang, W.-J. Zhang, S. Miki, T. Yamashita, H. Terai, X. Jiang, T.-Y. Chen, L.-X. You, X.-F. Chen, Z. Wang, J.-Y. Fan, Q. Zhang, and J.-W. Pan, "Quantum teleportation with independent sources and prior entanglement distribution over a network," Nat. Photonics **10**, 671–675 (2016).
27. H. Liu, C. Jiang, H.-T. Zhu, M. Zou, Z.-W. Yu, X.-L. Hu, H. Xu, S. Ma, Z. Han, J.-P. Chen, Y. Dai, S.-B. Tang, W. Zhang, H. Li, L. You, Z. Wang, Y. Hua, H. Hu, H. Zhang, F. Zhou, Q. Zhang, X.-B. Wang, T.-Y. Chen, and J.-W. Pan, "Field test of twin-field quantum key distribution through sending-or-not-sending over 428 km," Phys. Rev. Lett. **126**, 250502 (2021).
28. J.-P. Chen, C. Zhang, Y. Liu, C. Jiang, W.-J. Zhang, Z.-Y. Han, S.-Z. Ma, X.-L. Hu, Y.-H. Li, H. Liu, F. Zhou, H.-F. Jiang, T.-Y. Chen, H. Li, L.-X. You, Z. Wang, X.-B. Wang, Q. Zhang, and J.-W. Pan, "Twin-field quantum key distribution over a 511 km optical fibre linking two distant metropolitan areas," Nat. Photonics **15**, 570–575 (2021).
29. E. Saglamyurek, M. G. Puigibert, Q. Zhou, L. Giner, F. Marsili, V. B. Verma, S. W. Nam, L. Oesterling, D. Nippa, D. Oblak, and W. Tittel, "A multiplexed light-matter interface for fibre-based quantum networks," Nat. Commun. **7**, 11202 (2016).
30. Z. Zhang, C. Yuan, S. Shen, H. Yu, R. Zhang, H. Wang, H. Li, Y. Wang, G. Deng, Z. Wang, L. You, Z. Wang, H. Song, G.-C. Guo, and Q. Zhou, "High-performance quantum entanglement generation via cascaded second-order nonlinear processes," npj Quantum Inf. **7**, 1 (2021).
31. K. Wei, W. Li, H. Tan, Y. Li, H. Min, W.-J. Zhang, H. Li, L. You, Z. Wang, X. Jiang, T.-Y. Chen, S.-K. Liao, C.-Z. Peng, F. Xu, and J.-W. Pan, "High-speed measurement-device-independent quantum key distribution with integrated silicon photonics," Phys. Rev. X **10**, 031030 (2020).
32. E. Knill, R. Laflamme, and G. J. Milburn, "A scheme for efficient quantum computation with linear optics," Nature **409**, 46–52 (2001).
33. J. Lin, F. Bo, Y. Cheng, and J. Xu, "Advances in on-chip photonic devices based on lithium niobate on insulator," Photon. Res. **8**, 1910–1936 (2020).
34. S. Saravi, T. Pertsch, and F. Setzpfandt, "Lithium niobate on insulator: an emerging platform for integrated quantum photonics," Adv. Opt. Mater. **9**, 2100789 (2021).
35. D. Zhu, L. Shao, M. Yu, R. Cheng, B. Desiatov, C. Xin, Y. Hu, J. Holzgrafe, S. Ghosh, A. Shams-Ansari, E. Puma, N. Sinclair, C. Reimer, M. Zhang, and M. Lončar, "Integrated photonics on thin-film lithium niobate," Adv. Opt. Photonics **13**, 242–352 (2021).
36. S. Aghaeimeibodi, B. Desiatov, J.-H. Kim, C.-M. Lee, M. A. Buyukkaya, A. Karasahin, C. J. Richardson, R. P. Leavitt, M. Lončar, and E. Waks, "Integration of quantum dots with lithium niobate photonics," Appl. Phys. Lett. **113**, 221102 (2018).
37. J. Zhang, G. Muliuk, J. Juvert, S. Kumari, J. Goyvaerts, B. Haq, C. Op de Beeck, B. Kuyken, G. Morthier, D. Van Thourhout, A. Gocalinska, J. O'Callaghan, E. Pelucchi, K. Thomas, B. Corbett, A. J. Trindade, and G. Roelkens, "III-V-on-Si photonic integrated circuits realized using micro-transfer-printing," APL Photonics **4**, 110803 (2019).
38. Z. Ma, J.-Y. Chen, Z. Li, C. Tang, Y. M. Sua, H. Fan, and Y.-P. Huang, "Ultrabright quantum photon sources on chip," Phys. Rev. Lett. **125**, 263602 (2020).
39. J. Zhao, C. Ma, M. Rüsing, and S. Mookherjea, "High quality entangled photon pair generation in periodically poled thin-film lithium niobate waveguides," Phys. Rev. Lett. **124**, 163603 (2020).
40. G.-T. Xue, Y.-F. Niu, X. Liu, J.-C. Duan, W. Chen, Y. Pan, K. Jia, X. Wang, H.-Y. Liu, Y. Zhang, P. Xu, G. Zhao, X. Cai, Y.-X. Gong, X. Hu, Z. Xie, and S. Zhu, "Ultrabright multiplexed energy-time-entangled photon generation from lithium niobate on insulator chip," Phys. Rev. Appl. **15**, 064059 (2021).
41. S. Arahira, N. Namekata, T. Kishimoto, and S. Inoue, "Experimental studies in generation of high-purity photon-pairs using cascaded $\chi^{(2)}$ processes in a periodically poled $LiNbO_3$ ridge-waveguide device," J. Opt. Soc. Am. B **29**, 434–442 (2012).
42. B. S. Elkus, K. Abdelsalam, S. Fathpour, P. Kumar, and G. S. Kanter, "Quantum-correlated photon-pair generation via cascaded nonlinearity in an ultra-compact lithium-niobate nano-waveguide," Opt. Express **28**, 39963–39975 (2020).
43. M. R. Billah, M. Blaicher, T. Hoose, P.-I. Dietrich, P. Marin-Palomo, N. Lindenmann, A. Nesic, A. Hofmann, U. Troppenz, M. Moehrle, S. Randel, W. Freude, and C. Koos, "Hybrid integration of silicon photonics circuits and InP lasers by photonic wire bonding," Optica **5**, 876–883 (2018).
44. N. Lindenmann, G. Balthasar, D. Hillerkuss, R. Schmogrow, M. Jordan, J. Leuthold, W. Freude, and C. Koos, "Photonic wire bonding: a novel concept for chip-scale interconnects," Opt. Express **20**, 17667–17677 (2012).
45. M. He, M. Xu, Y. Ren, J. Jian, Z. Ruan, Y. Xu, S. Gao, S. Sun, X. Wen, L. Zhou, L. Liu, C. Guo, H. Chen, S. Yu, L. Liu, and X. Cai, "High-performance hybrid silicon and lithium niobate Mach–Zehnder modulators for 100 Gbit $s^{-1}$ and beyond," Nat. Photonics **13**, 359–364 (2019).
46. H. Okayama and M. Kawahara, "Waveguide array grating wavelength demultiplexer on $LiNbO_3$," in *Integrated Photonics Research* (Optical Society of America, 1995), paper ISaB3.
47. W. Ji, Z. Gong, R. Yin, J. Li, J. Li, L. Lv, and Q. Huang, "Tunable arrayed waveguide grating optical filter based on lithium niobate-on-insulator and electro-optic effect," Opt. Eng. **57**, 077102 (2018).
48. M. Prost, G. Liu, and S. B. Yoo, "A compact thin-film lithium niobate platform with arrayed waveguide gratings and MMIS," in *Optical Fiber Communications Conference and Exposition (OFC)* (IEEE, 2018), pp. 1–3.
49. H. Li and X. Cai, "Flat-top CWDM using narrow straight directional couplers on LN thin film," in *Asia Communications and Photonics Conference (ACP) and International Conference on Information Photonics and Optical Communications (IPOC)* (IEEE, 2020), pp. 1–3.
50. J.-X. Zhou, R.-H. Gao, J.-T. Lin, M. Wang, W. Chu, W.-B. Li, D.-F. Yin, L. Deng, Z.-W. Fang, J.-H. Zhang, R.-B. Wu, and Y. Cheng, "Electro-optically switchable optical true delay lines of meter-scale lengths fabricated on lithium niobate on insulator using photolithography assisted chemo-mechanical etching," Chin. Phys. Lett. **37**, 084201 (2020).
51. E. Lomonte, M. A. Wolff, F. Beutel, S. Ferrari, C. Schuck, W. H. Pernice, and F. Lenzini, "Single-photon detection and cryogenic reconfigurability in lithium niobate nanophotonic circuits," Nat. Commun. **12**, 6847 (2021).

52. A. A. Sayem, R. Cheng, S. Wang, and H. X. Tang, "Lithium-niobate-on-insulator waveguide-integrated superconducting nanowire single-photon detectors," Appl. Phys. Lett. **116**, 151102 (2020).
53. A. Aimone, F. Frey, R. Elschner, I. G. Lopez, G. Fiol, P. Rito, M. Gruner, A. Ulusoy, D. Kissinger, J. Fischer, C. Schubert, and M. Schell, "DAC-less 32-GBd PDM-256-QAM using low-power InP IQ segmented MZM," IEEE Photonics Technol. Lett. **29**, 221–223 (2016).
54. C. Wang, M. Zhang, X. Chen, M. Bertrand, A. Shams-Ansari, S. Chandrasekhar, P. Winzer, and M. Lončar, "Integrated lithium niobate electro-optic modulators operating at CMOS-compatible voltages," Nature **562**, 101–104 (2018).
55. M. Zhang, B. Buscaino, C. Wang, A. Shams-Ansari, C. Reimer, R. Zhu, J. M. Kahn, and M. Lončar, "Broadband electro-optic frequency comb generation in a lithium niobate microring resonator," Nature **568**, 373–377 (2019).
56. Y. Hu, M. Yu, D. Zhu, N. Sinclair, A. Shams-Ansari, L. Shao, J. Holzgrafe, E. Puma, M. Zhang, and M. Lončar, "On-chip electro-optic frequency shifters and beam splitters," Nature **599**, 587–593 (2021).
57. R. H. Brown and R. Q. Twiss, "Correlation between photons in two coherent beams of light," Nature **177**, 27–29 (1956).
58. R. Kumar, J. R. Ong, M. Savanier, and S. Mookherjea, "Controlling the spectrum of photons generated on a silicon nanophotonic chip," Nat. Commun. **5**, 5489 (2014).
59. R.-B. Jin, R. Shimizu, K. Wakui, H. Benichi, and M. Sasaki, "Widely tunable single photon source with high purity at telecom wavelength," Opt. Express **21**, 10659–10666 (2013).
60. R.-B. Jin, J. Zhang, R. Shimizu, N. Matsuda, Y. Mitsumori, H. Kosaka, and K. Edamatsu, "High-visibility nonclassical interference between intrinsically pure heralded single photons and photons from a weak coherent field," Phys. Rev. A **83**, 031805 (2011).
61. X. Li, L. Yang, L. Cui, Z. Y. Ou, and D. Yu, "Observation of quantum interference between a single-photon state and a thermal state generated in optical fibers," Opt. Express **16**, 12505–12510 (2008).
62. A. I. Lvovsky and M. G. Raymer, "Continuous-variable optical quantum-state tomography," Rev. Mod. Opt. **81**, 299–332 (2009).
63. T. Pittman, B. Jacobs, and J. Franson, "Experimental demonstration of a quantum circuit using linear optics gates," Phys. Rev. A **71**, 032307 (2005).
64. H. Fearn and R. Loudon, "Theory of two-photon interference," J. Opt. Soc. Am. B **6**, 917–927 (1989).
65. J. Rarity, P. Tapster, and R. Loudon, "Non-classical interference between independent sources," J. Opt. B **7**, S171–S175 (2005).
66. T. Miyazawa, K. Takemoto, Y. Nambu, S. Miki, T. Yamashita, H. Terai, M. Fujiwara, M. Sasaki, Y. Sakuma, M. Takatsu, T. Yamamoto, and Y. Arakawa, "Single-photon emission at 1.5 μm from an InAs/InP quantum dot with highly suppressed multi-photon emission probabilities," Appl. Phys. Lett. **109**, 132106 (2016).
67. Ł. Dusanowski, M. Syperek, J. Misiewicz, A. Somers, S. Hoefling, M. Kamp, J. Reithmaier, and G. Sek, "Single-photon emission of InAs/InP quantum dashes at 1.55 μm and temperatures up to 80 K," Appl. Phys. Lett. **108**, 163108 (2016).
68. L. Schweickert, K. D. Jöns, K. D. Zeuner, S. F. Covre da Silva, H. Huang, T. Lettner, M. Reindl, J. Zichi, R. Trotta, A. Rastelli, and V. Zwiller, "On-demand generation of background-free single photons from a solid-state source," Appl. Phys. Lett. **112**, 093106 (2018).
69. H. Wang, Y.-M. He, T.-H. Chung, H. Hu, Y. Yu, S. Chen, X. Ding, M.-C. Chen, J. Qin, X. Yang, R.-Z. Liu, Z.-C. Duan, J.-P. Li, S. Gerhardt, K. Winkler, J. Jurkat, L.-J. Wang, N. Gregersen, Y.-H. Huo, Q. Dai, S. Yu, S. Höfling, C.-Y. Lu, and J.-W. Pan, "Towards optimal single-photon sources from polarized microcavities," Nat. Photonics **13**, 770–775 (2019).
70. S. K. Joshi, D. Aktas, S. Wengerowsky, M. Lončarić, S. P. Neumann, B. Liu, T. Scheidl, G. C. Lorenzo, Ž. Samec, L. Kling, A. Qiu, M. Razavi, M. Stipčević, J. G. Rarity, and R. Ursin, "A trusted node–free eight-user metropolitan quantum communication network," Sci. Adv. **6**, eaba0959 (2020).
71. H. Zou and H. Wang, "Pulse-forming-line based on-chip short pulse generator," Rev. Sci. Instrum. **86**, 044706 (2015).
72. Z. Fu and H. Liu, "Ultra-narrow pulse generator with precision-adjustable pulse width," Rev. Sci. Instrum. **89**, 055103 (2018).
73. Z. Ou, "Quantum theory of fourth-order interference," Phys. Rev. A **37**, 1607–1619 (1988).
74. F. Sun and C. Wong, "Indistinguishability of independent single photons," Phys. Rev. A **79**, 013824 (2009).
75. M. Avenhaus, H. B. Coldenstrodt-Ronge, K. Laiho, W. Mauerer, I. A. Walmsley, and C. Silberhorn, "Photon number statistics of multimode parametric down-conversion," Phys. Rev. Lett. **101**, 053601 (2008).